

Activation energies for two steps in the S_2 → S_3 transition of photosynthetic water oxidation from time-resolved single- frequency infrared spectroscopy

Cite as: J. Chem. Phys. **153**, 215101 (2020); <https://doi.org/10.1063/5.0027995>

Submitted: 01 September 2020 . Accepted: 05 November 2020 . Published Online: 01 December 2020

 Sarah M. Mäusle,  Aiganym Abzaliyeva,  Paul Greife,  Philipp S. Simon,  Rebeca Perez,  Yvonne Zilliges, and  Holger Dau

COLLECTIONS

Paper published as part of the special topic on [65 Years of Electron Transfer](#)



View Online



Export Citation



CrossMark

ARTICLES YOU MAY BE INTERESTED IN

[Reflections on electron transfer theory](#)

The Journal of Chemical Physics **153**, 210401 (2020); <https://doi.org/10.1063/5.0035434>

[Combining the best of two worlds: Stimulated Raman excited fluorescence](#)

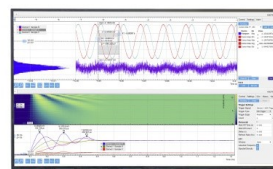
The Journal of Chemical Physics **153**, 210901 (2020); <https://doi.org/10.1063/5.0030204>

[Removing artifacts in polarizable embedding calculations of one- and two-photon absorption spectra of fluorescent proteins](#)

The Journal of Chemical Physics **153**, 215102 (2020); <https://doi.org/10.1063/5.0023434>

Challenge us.

What are your needs for
periodic signal detection?



Zurich
Instruments

Activation energies for two steps in the $S_2 \rightarrow S_3$ transition of photosynthetic water oxidation from time-resolved single-frequency infrared spectroscopy

Cite as: J. Chem. Phys. 153, 215101 (2020); doi: 10.1063/5.0027995

Submitted: 1 September 2020 • Accepted: 5 November 2020 •

Published Online: 1 December 2020



View Online



Export Citation



CrossMark

Sarah M. Mäusle,  Aiganyam Abzaliyeva,  Paul Greife,  Philipp S. Simon,  Rebeca Perez, 
Yvonne Zilliges,  and Holger Dau^{a)} 

AFFILIATIONS

Department of Physics, Freie Universität Berlin, Arnimallee 14, 14195 Berlin, Germany

Note: This paper is part of the JCP Special Topic on 65 Years of Electron Transfer.

^{a)} Author to whom correspondence should be addressed: holger.dau@fu-berlin.de

ABSTRACT

The mechanism of water oxidation by the Photosystem II (PSII) protein-cofactor complex is of high interest, but specifically, the crucial coupling of protonation dynamics to electron transfer (ET) and dioxygen chemistry remains insufficiently understood. We drove spinach-PSII membranes by nanosecond-laser flashes synchronously through the water-oxidation cycle and traced the PSII processes by time-resolved single-frequency infrared (IR) spectroscopy in the spectral range of symmetric carboxylate vibrations of protein side chains. After the collection of IR-transients from 100 ns to 1 s, we analyzed the proton-removal step in the $S_2 \Rightarrow S_3$ transition, which precedes the ET that oxidizes the Mn_4CaO_x -cluster. Around 1400 cm^{-1} , pronounced changes in the IR-transients reflect this pre-ET process ($\sim 40\ \mu\text{s}$ at 20°C) and the ET step ($\sim 300\ \mu\text{s}$ at 20°C). For transients collected at various temperatures, unconstrained multi-exponential simulations did not provide a coherent set of time constants, but constraining the ET time constants to previously determined values solved the parameter correlation problem and resulted in an exceptionally high activation energy of $540 \pm 30\text{ meV}$ for the pre-ET step. We assign the pre-ET step to deprotonation of a group that is re-protonated by accepting a proton from the substrate-water, which binds concurrently with the ET step. The analyzed IR-transients disfavor carboxylic-acid deprotonation in the pre-ET step. Temperature-dependent amplitudes suggest thermal equilibria that determine how strongly the proton-removal step is reflected in the IR-transients. Unexpectedly, the proton-removal step is only weakly reflected in the 1400 cm^{-1} transients of PSII core complexes of a thermophilic cyanobacterium (*T. elongatus*).

Published under license by AIP Publishing. <https://doi.org/10.1063/5.0027995>

I. INTRODUCTION

Photosystem II (PSII) is a large protein complex situated in the thylakoid membrane of plants and cyanobacteria and is the site of oxidative water splitting.^{1–5} The capability of PSII to utilize water as a raw material when converting solar energy into chemical energy has fascinated researchers for many years, for various reasons: As the main source of oxygen in our atmosphere, PSII provides the basis for higher life on Earth. Furthermore, mimicking the PSII capabilities

may become the basis of a sustainable route of renewable, non-fossil fuels.^{6–8}

In PSII, following the absorption of a photon, the primary charge separation event takes place at the PSII reaction center comprising four chlorophylls and two pheophytins [Fig. 1(a)]. An electron is removed from P680 within picoseconds by reducing the neighboring pheophytin molecule. From there, the electron moves on via the primary quinone acceptor, Q_A , to the secondary quinone acceptor, Q_B , which, once doubly reduced, leaves its

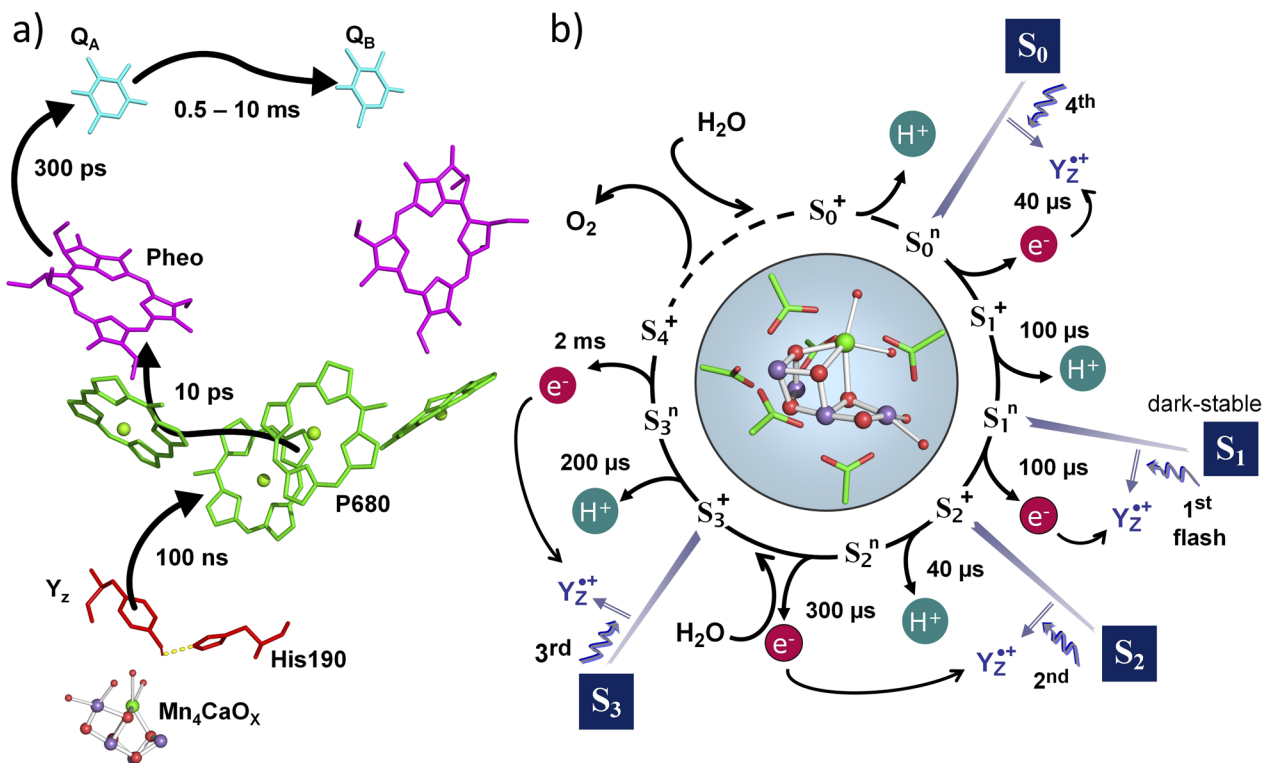


FIG. 1. Light-driven redox processes in Photosystem II. (a) Scheme of redox factors and cascade of electron-transfer reactions. After absorption of a light quantum (photon) by the antenna pigment of PSII (not shown), P680 is oxidized by electron transfer (ET) to a pheophytin (Pheo), a quinone (Q_B), and a secondary quinone acceptor (Q_A), with the latter possibly involving non-heme Fe¹⁷ (not shown). P680⁺ returns to its neutral state with the donation of an electron from a redox-active tyrosine, Tyr 160 of the D1 protein of PSII (Y_Z). (b) Extended S-state cycle illustrating the alternating oxidation and proton release events of photosynthetic water oxidation.^{9,15,18} Starting from the dark stable S₁ⁿ state, four light flashes drive Y_Z oxidation, which is largely completed within 100 ns after the flash. The formation of Y_Z^{ox} is coupled to the movement of the tyrosine proton to a neighboring histidine (D1-His 190), thereby maintaining a positive charge close to Y_Z (thus, Y_Z^{ox}). An electron transferred from the Mn₄CaO_x cluster, pictured in the center with surrounding carboxylate ligands, returns Y_Z^{ox} back to its reduced form. The two "substrate" water molecules likely bind to the Mn₄CaO_x cluster during the S₂ → S₃ and S₃ → S₀ transitions. Protons are removed from the Mn₄CaO_x environment toward the aqueous bulk; internal proton movements are not considered. The indicated times represent reciprocal rate constants and are approximate room-temperature values. The depicted structures in (a) and (b) were rendered in PyMOL using the 6DHE structure¹⁹ from the Protein Data Bank.

binding pocket as a hydroquinone (QH₂) and is replaced by a "fresh" Q_B in its oxidized state. The electron hole at P680 is meanwhile filled by electron donation from a redox-active tyrosine residue, Y_Z, which is, in turn, reduced by oxidizing one of the manganese ions of the Mn₄CaO_x cluster^{2–5,9,10} bound to the D1 (PsbA) and CP43 (PsbC) subunits of PSII.^{11–13} This process is repeated four times, allowing the accumulation of the four oxidative equivalents needed for water oxidation. The Mn₄CaO_x cluster is thus capable of coupling one-electron photochemistry with a four-electron redox reaction. The oxidation states of the Mn₄CaO_x cluster are denoted as S-states, S₀ to S₄, where subscript indicates the number of accumulated oxidative equivalents. While four S-states are stable or at least semi-stable, the S₄ state is merely transiently formed, directly followed by O–O bond formation and O₂ release, during which the Mn₄CaO_x cluster returns back to its most reduced state (S₀).^{14–16}

This four-step process was first visible in data of Joliot *et al.*,¹⁴ soon followed by the development of the basic S-state cycle model

by Kok *et al.*,²⁰ and since then, it has been extensively studied. It was shown that the electron transfer (ET) steps are intermitted by proton transfer (PT) steps,^{21–23} which prevents an increase in the overall charge and thus in the redox potential of the Mn₄CaO_x cluster [Fig. 1(b)]. Throughout the cycle, two water insertion events take place, replacing the two substrate water molecules that had been oxidized in a previous turnover of the reaction cycle. Today, it is the general consensus that the water molecules are inserted during the S₂ → S₃ and the S₃ → S₀ transition,^{19,24–27} although the exact timing and sequence of events are still under debate.

The general structure of PSII with bound Mn ions was first resolved in 2001 by Zouni *et al.*¹¹ using x-ray crystallography; later, more highly resolved structures^{13,28–30} and structures of various intermediate states of the water oxidation cycle followed.^{19,31–33} Recent crystallography studies at room temperature using x-ray free electron laser (XFEL) radiation^{19,26,34} have been informative regarding the water insertion at the Mn₄CaO_x cluster and the movement of various amino acid residues and protein-internal water molecules,

which may support identification of substrate–water insertion pathways. Even though some of these studies show structures at different points in time after the excitation flash, the time resolution is limited (structural snapshots are available only for a small number of points in time), hindering an analysis of the reaction kinetics. Furthermore, the observation of protons is not directly possible. Complementary spectroscopic investigation is therefore necessary for a full understanding of the mechanistic details of the S-state cycle.

Infrared (IR) difference spectroscopy allows for tracking structural changes, including changes in hydrogen-bonding, and protonation state changes.³⁵ Fourier-transform infrared (FTIR) spectroscopic measurements of PSII have been used to characterize such structural changes,^{36–39} while time-resolved single-frequency IR (TRSF-IR) studies are proving to be a good addition to help shed light into the kinetics of the S-state cycle,⁴⁰ including proton movement. The Mn_4CaO_x cluster has several amino-acid ligands containing carboxylate groups (i.e., aspartate and glutamate side chains) in its closer vicinity (first-coordination sphere ligands and more distant ligands). Even though a clear assignment of carboxylate bands to individual amino acid residues has so far mostly been unsuccessful, the symmetric carboxylate stretching mode has still been shown to be well-suited for observing events of the S-state-cycle with FTIR.^{36,41,42} Noguchi and co-workers have also shown that time-resolved IR data at 1400 cm^{-1} can give insight into reaction kinetics and likely mechanisms of the individual S-state transitions,⁴⁰ specifically for the $\text{S}_2 \rightarrow \text{S}_3$ transition.^{43,44}

The Mn_4CaO_x cluster has an excess positive charge in the S_2 -state,⁴⁵ which needs to be removed before Mn oxidation can take place.^{9,21} This charge removal proceeds by relocation of a proton to the aqueous bulk before the start of the electron transfer to Y_Z^{ox} .^{22,46} Electron paramagnetic resonance (EPR) studies^{47–50} have shown that two isomers of the Mn_4CaO_x cluster exist in the S_2 -state: an open-cubane (low-spin) and a closed-cubane structure (high-spin). It has been suggested that a structural rearrangement from one isomeric form into the other is needed for the advancement into the S_3 -state.^{10,51–53} A recent crystallographic study of the $\text{S}_2 \rightarrow \text{S}_3$ transition by Ibrahim *et al.*²⁶ did not find any evidence of the closed-cubane structure at the time-points that they probed, but they cannot exclude that a low population of that isomer might be present. Depending on the isomeric form the Mn_4CaO_x cluster adopts before transitioning into the S_3 -state, different mechanisms regarding water insertion and Mn oxidation have been suggested.^{3,54}

The activation energy of the redox steps of the individual S-state transitions has been observed for plant PSII membrane particles prepared from spinach leaves by Renger and Hanssum⁵⁵ or for pea seedlings by Haumann *et al.*;⁵⁶ the activation energy was found to be clearly larger for the $\text{S}_2 \rightarrow \text{S}_3$ transition than for other S-state transitions. Klauss *et al.*²² observed that a proton transfer step (PT) in the $\text{S}_2 \rightarrow \text{S}_3$ transition has an even higher activation energy, as well as a large $\text{H}_2\text{O}/\text{D}_2\text{O}$ kinetic isotope effect (KIE) of 5.6. (Rather than being a specific local PT step, the process investigated by Klauss *et al.*²² accounts for the removal of a proton in the vicinity of the Mn_4CaO_x cluster of PSII by deprotonation of a still unknown group, transfer of the proton to the PSII periphery, and eventually release into the aqueous bulk, and thus, it has been referred to as a proton removal step.^{9,15,18}) Noguchi and

co-workers,⁴³ however, did not observe such a large KIE in their single-frequency IR study of PSII core particles from *T. elongatus*. (Here and in the following, we denote the energy value determined from an Arrhenius plot of the temperature dependence of the time constants as “activation energy.” In terms of transition-state theory, the here discussed activation energy corresponds to the enthalpy of activation.)

In the present study, we investigate the events of the $\text{S}_2 \rightarrow \text{S}_3$ transition by monitoring the flash-induced IR absorption changes at 1400 cm^{-1} and 1395 cm^{-1} , at various temperatures. We address drawbacks of an unbiased multi-exponential analysis and describe a knowledge-biased simulation approach that eventually facilitated a meaningful analysis of the IR transients, resulting in an activation energy of the proton removal step that is consistent with the results of Klauss *et al.* obtained by photothermal beam deflection (PBD) experiments.^{22,23} Furthermore, we demonstrate surprising differences between IR time traces of PSII membrane particles from spinach and PSII core particles from the thermophilic cyanobacterium *T. elongatus*. The results are comprehensively discussed in the context of early and recent results on the $\text{S}_2 \rightarrow \text{S}_3$ transition of photosynthetic water oxidation.

II. MATERIAL AND METHODS

A. Preparation of spinach PSII membrane particles

PSII membrane particles were isolated from spinach following a protocol described elsewhere⁵⁷ modified from the original by Berthold, Babcock, and Yocum⁵⁸ and stored in a buffer (pH 6.2) containing 1M betaine, 25 mM MES, 15 mM NaCl, 5 mM MgCl_2 , and 5 mM CaCl_2 at $-80\text{ }^\circ\text{C}$ until usage. The sample was probed for its intactness by measuring its oxygen evolution activity with a Clarke-type electrode at $28\text{ }^\circ\text{C}$ using a sample amount of $10\text{ }\mu\text{g}$ Chl, as well as $250\text{ }\mu\text{M}$ DCBQ and 1 mM $\text{K}_3[\text{Fe}(\text{CN})_6]$ as electron acceptors, yielding $900\text{ }\mu\text{mol}$ – $950\text{ }\mu\text{mol}$ $\text{O}_2/(\text{mg Chl})/\text{h}$. Before a measurement, the sample (corresponding to about 2 mg of chlorophyll) was left to thaw on ice and subsequently exchanged into the same buffer without betaine. The buffer exchange was performed by centrifuging the sample at $50,000\text{ g}$ for 12 min, decanting the supernatant, and resuspending in the new buffer. After repeating the centrifugation, the resulting soft pellet was transferred to CaF_2 plates with a spatula. PPBQ (phenyl-*p*-benzoquinone) was added as an artificial electron acceptor. The sample was sealed between 3 to 4 pairs of CaF_2 plates using a small amount of silicon grease and $15\text{ }\mu\text{m}$ PTFE spacers. The CaF_2 plates were then mounted onto the sample holder. The sample was kept in the dark at all times, and all work was done under dim green light.

B. Purification of *T. elongatus* PSII core complexes

The PSII core complexes (PSIIccs) were purified from *T. elongatus* WT* cells, a strain that has a deletion of the *psbD2* gene and a His-tag on the C-terminal end of CP43. *T. elongatus* WT* cells were grown at continuous illumination at $48\text{ }^\circ\text{C}$ in a BG11 medium. The cells were harvested after the culture reached a final OD of 1.6. The thylakoid membranes were extracted from the cells by lysozyme digestion followed by cell disruption using a cell disruption vessel (Parr Instrument) at 30 atm nitrogen pressure

and osmotic shock, as described previously.⁵⁹ The thylakoid membranes were resuspended in a buffer (20 mM MES pH 6.0, 10 mM MgCl₂, 10 mM MgCl₂, 5 mM CaCl₂, and 100 mM betaine) at a Chl concentration of 1 mg/ml and solubilized by incubation with 1% (w/v) *n*-dodecyl- β -maltoside, 0.25 mM Pefabloc (Sigma-Aldrich), and 1x protease at 4 °C for 1 h under slow rotation. The suspension was centrifuged (20 min, 170 000 g), and the supernatant containing PSII core complexes bound to a nickel resin. The PSSIIccs were eluted with 200 mM L-histidine and subsequently concentrated using Amicon Ultra-15 concentrator devices (Millipore) with a 100 kDa cutoff, as described by Sugiura *et al.*⁶⁰ PSIIccs were stored in liquid nitrogen at a concentration of 2.76 mg Chl ml⁻¹ in 40 mM MES (pH 6), 10 mM CaCl₂, 10 mM MgCl₂, 100 mM betaine, 0.04% β -DM, and 10% glycerol. The oxygen activity of the PSIIcc was 2478 mmol/(mg h).

Before an IR measurement, the PSIIcc sample corresponding to 200 μ g Chl was thawed on ice. The sample was exchanged into the measurement buffer containing 10 mM MES, 5 mM CaCl₂, 5 mM NaCl, 0.06% (w/v) *n*-dodecyl β -D-maltoside, and 400 mM sucrose (adapted from Ref. 61) using Bio-Gel P-6 columns (Bio-Rad). Potassium ferricyanide was added as an artificial electron acceptor to a final concentration of 10 mM.

C. Measurement of IR transients

The time-resolved single-frequency infrared (TRSF-IR) measurements were performed with a custom-built setup using a mid-IR quantum-cascade laser (QCL) as a continuous single-frequency IR source, tunable to frequencies between 1300 cm⁻¹ and 1650 cm⁻¹ (Daylight Solutions, San Diego, CA). A 5 ns frequency-doubled 532 nm Nd:YAG laser (Continuum, Milpitas, CA) was used as an excitation laser. A self-built x-y-movable sample holder allows for automated sample exchange. Figure S1 of the [supplementary material](#) shows a scheme of the experimental procedure. The IR beam is focused on a small spot on the CaF₂ plate, and the transmitted light is measured with a 10 MHz pre-amplified mercury cadmium telluride (MCT) detector (Vigo Systems, Poland) and recorded with a 16-bit A/D converter at a sampling rate of 65 MS/s (Spectrum, Germany). Upon moving to a new sample spot, the IR signal of the dark-adapted PSII is measured for a few seconds before a series of coincident saturating laser flashes are applied to the sample spot with a flash spacing of 1 s. By modification of the delay time between the laser flash lamp and the Q-switch, the energy of the tenth and final laser flash was tripled; the thereby obtained IR transient was later used for the correction of the laser-induced heat artifact in a similar way as reported by Noguchi and co-workers⁴³ (see Fig. S2 of the [supplementary material](#) for a detailed description). After the flash sequence is completed, the sample holder moves a fresh sample spot into the beam focus. The number of total sample spots was chosen such that there was minimally 1 h of dark-adaption before a specific spot was exposed again to the sequence of 10 laser flashes, resulting in roughly 200 unique positions. The chamber containing the sample holder was continuously purged with cooled dry air; the temperature was maintained at the desired value by using two Peltier elements connected to the sample chamber. Temperature probes (ThorLabs, Newton, NJ) mounted onto the sample holder allowed for the determination of the sample temperature.

The experiments were performed at a pH of 6.2 at selected temperatures ranging from 5 °C to 30 °C. After mounting the samples, two saturating pre-flashes were applied followed by an hour of dark-adaption again before beginning the actual data collection.

D. Data analysis

Data analysis and simulations (fits) were performed employing a self-written Python code (Python 3.7, Python Software Foundation). IR data were collected with a sampling rate of 65 MHz and were binned to 200 data points per decade, resulting in equally spaced points on a logarithmic time axis (quasi-logarithmic averaging). For each of the reported IR transients, between 200 and 4000 individually collected transients were averaged (Table SII). All time courses displayed in this article are heat-artifact corrected, as described in the [supplementary material](#). The IR difference absorption is calculated (in mOD) by using the IR signal before each flash as a reference (see the [supplementary material](#) for more details).

To extract time constants from the time courses, the data were simulated with a multi-exponential function,

$$y_{sim}(t) = y_0 + \sum_i A_i * \left(1 - \exp\left(-\frac{t}{\tau_i}\right) \right), \quad (1)$$

where y_0 is the initial value, τ_i are the time constants, and A_i are the corresponding amplitudes. The simulation parameters were determined by a least-squares fit of the logarithmically averaged data.

III. RESULTS

A. Probing carboxylate bands at 1400 cm⁻¹ and 1395 cm⁻¹

To follow the events of the S-state cycle of PSII, we investigated the time-resolved IR signal of the symmetric carboxylate stretching band at 1400 cm⁻¹ and 1395 cm⁻¹. Figure 2(a) shows the steady-state IR values at 1400 cm⁻¹ as a function of the flash number, which exhibit a clear period-of-four oscillation. By simulating these flash patterns with a classic Kok four-population model,^{20,62} the miss-factor was estimated to be between 6% and 12%, with a tendency toward higher miss-factors at higher temperatures, which is in agreement with previous observations.^{43,63} The patterns look similar at almost all temperatures, except for the data at 27 °C, which show a significant drop in amplitude and a more dampened oscillation pattern, likely explainable by high-temperature deactivation of a significant fraction of the photosystems within the data collection period. This drop in the signal at high temperatures is observed for the steady state signal at both 1400 cm⁻¹ and 1395 cm⁻¹ (Fig. S4), and it is not reversed by lowering the temperature after completion of data collection at 27 °C (not shown).

Figure 2(b) shows the time courses at 1400 cm⁻¹ for the first four flashes at 11 °C. Assuming that in dark-adapted PSII the dark-stable S₁-state is populated preferentially, the first and second flash transients should trace predominately the S₁ \rightarrow S₂ and S₂ \rightarrow S₃ transitions, respectively. After the third flash, we already expect a significant mixing of S-states due to the miss-factor. In the following, we analyze the S₂ \rightarrow S₃ transition induced by the second flash, for

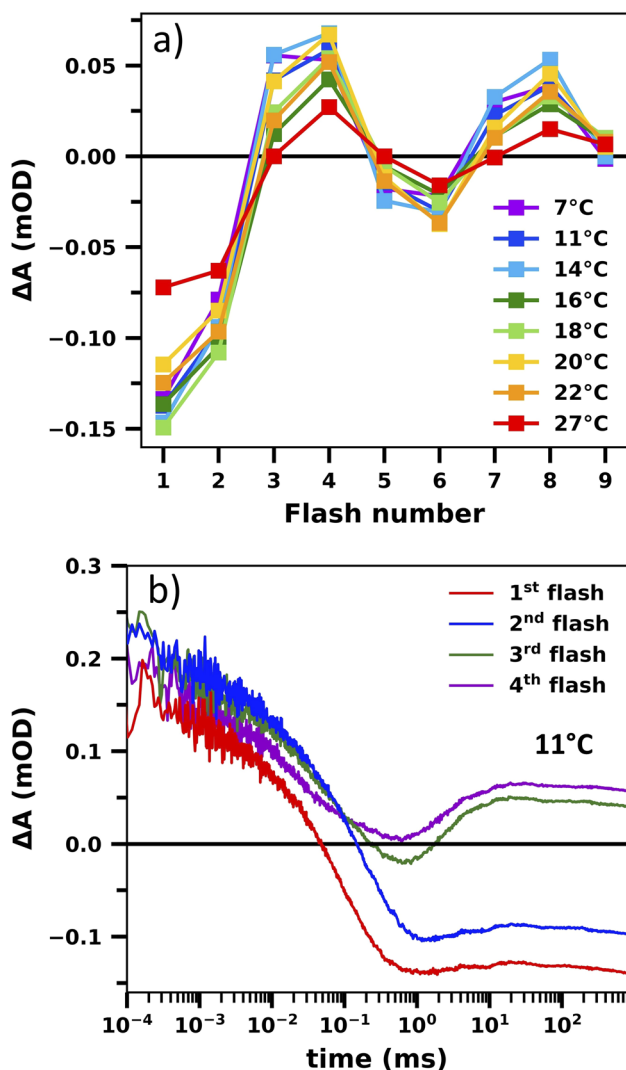


FIG. 2. Flash-number dependence of IR transients of PSII membrane particles from spinach at 1400 cm^{-1} . (a) Steady-state values at various temperatures as a function of the flash number. The steady-state values were obtained by averaging the last 400 ms of the transients. (b) Time-resolved IR transients at 1400 cm^{-1} for the first, second, third, and fourth flash applied to dark-adapted PSII measured at 11°C . The transients were corrected for an excitation flash-induced heat artifact (as described in the [supplementary material](#)). The corresponding data at 1395 cm^{-1} are shown in Fig. S3.

which the correction for the likely minor influence of S-state mixing is not required [see Fig. S10 for the influence of the S-state starting population and miss-factor estimation on the main results shown in Fig. 5(c)].

Figure 3 shows the time course for the second flash (from hereon referred to as the $S_2 \rightarrow S_3$ transition) at 7°C and at 18°C . When simulating the curves between $5\ \mu\text{s}$ and 30 ms with a sum of exponentials, visual inspection of the residuals (i.e., the difference between the measured and simulated absorption transients)

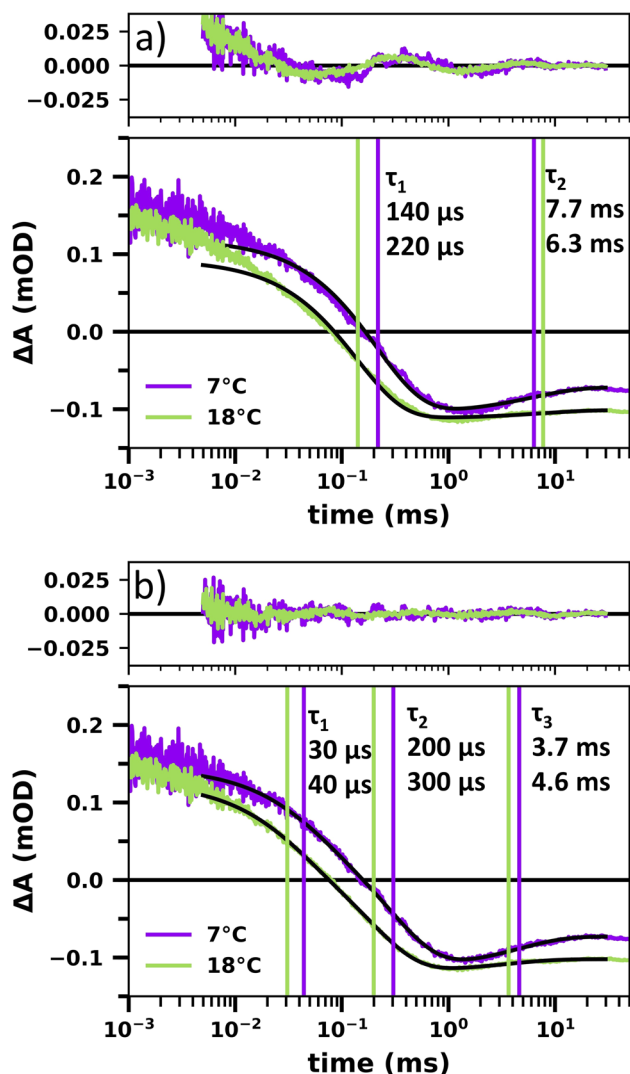


FIG. 3. IR-transients of PSII-enriched membrane particles from spinach at 1400 cm^{-1} measured at 7°C (purple) and at 18°C (green) after the second excitation flash. The transients were simulated with a sum of exponentials (black curves), and the resulting time constants are indicated by vertical lines. The residuals are shown above the transients. (a) Results of a simulation with two exponential components and an offset. (b) Results of a simulation with three exponential components and an offset.

reveals that a single decay component in the sub-millisecond regime is insufficient for a high-quality simulation [Fig. 3(a)]. With two decaying and one rising ms-component, however, the curve can be simulated well, as shown in Fig. 3(b). The millisecond component is detectable in the transients of all flash-induced transitions [see Fig. 2(b)]. It is assignable to the quinone reactions at the PSII acceptor side, which are not in the focus of the present investigation (Fig. S9). Its inclusion in the form of single-exponential rise allows for a high simulation quality covering a comparable large time range (more than 3 decades, $5\ \mu\text{s}$ up to 30 ms), thereby increasing the

significance for determination of the exponential components that describe the donor side events in the $S_2 \rightarrow S_3$ transition.

Following the excitation flash, $Q_A^- Y_Z^+$ is formed in the majority of PSII within less than 100 ns and thus not within the temporal resolution of our experiment. The electron transfer (ET) from the Mn_4CaO_x cluster to Y_Z^+ and its preceding proton transfer (PT) step, however, are expected to be visible in these data on the microsecond time scale. Based on the time constants determined in previous investigations,^{21–23,64,65} we assign the faster decaying phase to the PT step and the slower decaying to the ET step of the $S_2 \rightarrow S_3$ transition. The slow millisecond rise is most likely assignable to acceptor side kinetics since ET from Q_A to Q_B and Q_B binding are expected on this timescale,^{66–68} as supported by the time-resolved detection of the quinone CO/CC vibration⁶⁹ at 1478 cm^{-1} (Fig. S9).

The approach of simulating the transients with three exponential components was applied to the $S_2 \rightarrow S_3$ time courses at eight different temperatures at 1400 cm^{-1} and seven temperatures at 1395 cm^{-1} , as shown in Fig. 4(a) and Fig. S5(a), respectively. Figure 5(a) shows the Arrhenius plot of the resulting time constants, where τ_1 corresponds to the PT phase, τ_2 corresponds to the ET phase, and τ_3 corresponds to the slow millisecond-rise. While there is a clear trend of increasing time constants with decreasing temperatures, there is a discrepancy of the results for 1400 cm^{-1}

and 1395 cm^{-1} : for the ET phase, we get an activation energy of $280 \pm 60\text{ meV}$ at 1400 cm^{-1} but only $90 \pm 40\text{ meV}$ at 1395 cm^{-1} (see Table I); both values are clearly smaller than what have been previously reported.^{55,56}

The discrepancy between time constants retrieved from the simulation of the IR transients at 1395 cm^{-1} and 1400 cm^{-1} is problematic because we expect to observe the same events (and thus the same time constants) at both IR wavenumbers. The unsatisfactory fit results likely result from insufficient significance of the fit parameters. Therefore, we constrained the fits by fixing τ_2 to previously established values of the ET phase, with time constants and activation energy of the ET phase determined by Renger and Hanssum.⁵⁵ The corresponding simulations are shown in Fig. 4(b), for 1400 cm^{-1} , and Fig. S5(b), for 1395 cm^{-1} . Now, an almost identical Arrhenius plot for the PT phase is obtained for both wavenumbers [Fig. 5(c)]. The activation energy of the PT phase was determined to be $550 \pm 40\text{ meV}$ and $540 \pm 30\text{ meV}$ for 1400 cm^{-1} and 1395 cm^{-1} , respectively. These values are higher than the previously reported $470 \pm 50\text{ meV}$,²² but when considering an uncertainty of at least $\pm 50\text{ meV}$ for both studies, the values are still in agreement with each other. It should be noted that the fit quality decreases with the constrained approach, which can be seen in the residuals, especially below $10\text{ }\mu\text{s}$. For an extended fit range of 100 ns to 30 ms and inclusions of an additional fast time constant, the fit quality of the

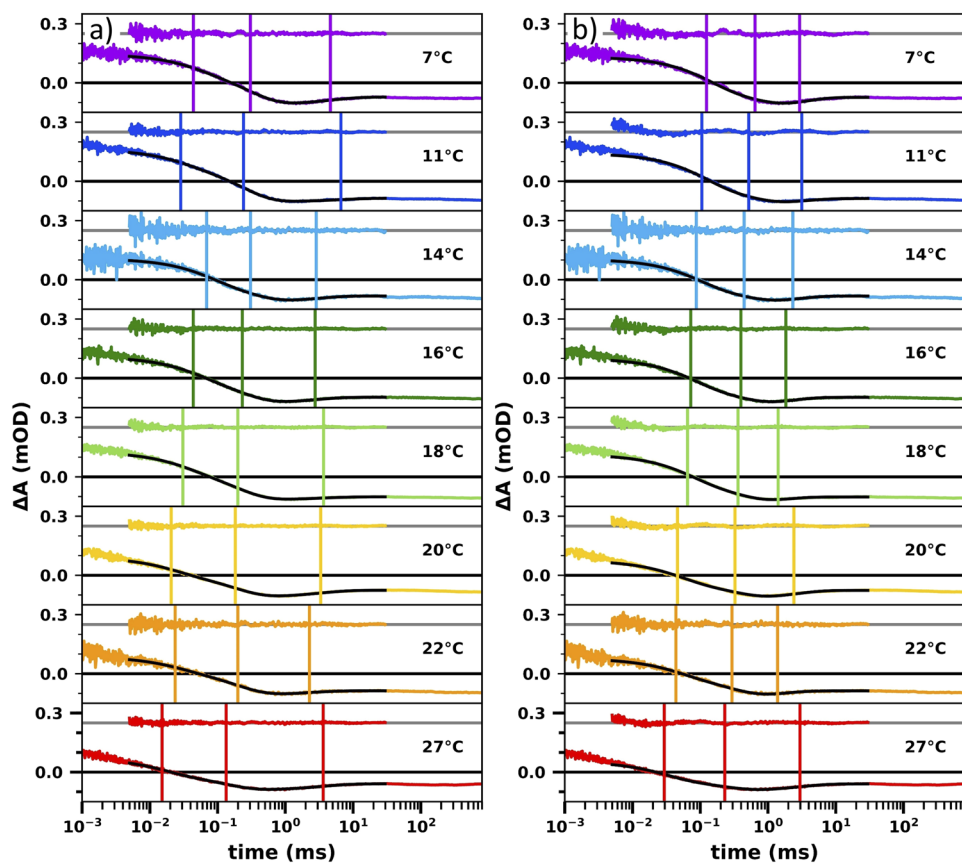


FIG. 4. IR transients of PSII-enriched membrane particles from spinach at 1400 cm^{-1} recorded after the second excitation flash ($S_2 \rightarrow S_3$) at various temperatures. The IR data were collected for a time range covering six decades but analyzed by curve-fitting between $5\text{ }\mu\text{s}$ and 30 ms . The time courses were simulated with a sum of three exponentials. The corresponding residuals are plotted above each time course; they were multiplied with a factor of 2 to allow for better visual inspection. (a) Unconstrained three-exponential fits. (b) Fits with τ_2 fixed to the temperature-dependent ET rate of the $S_2 \rightarrow S_3$ transition.⁵⁵

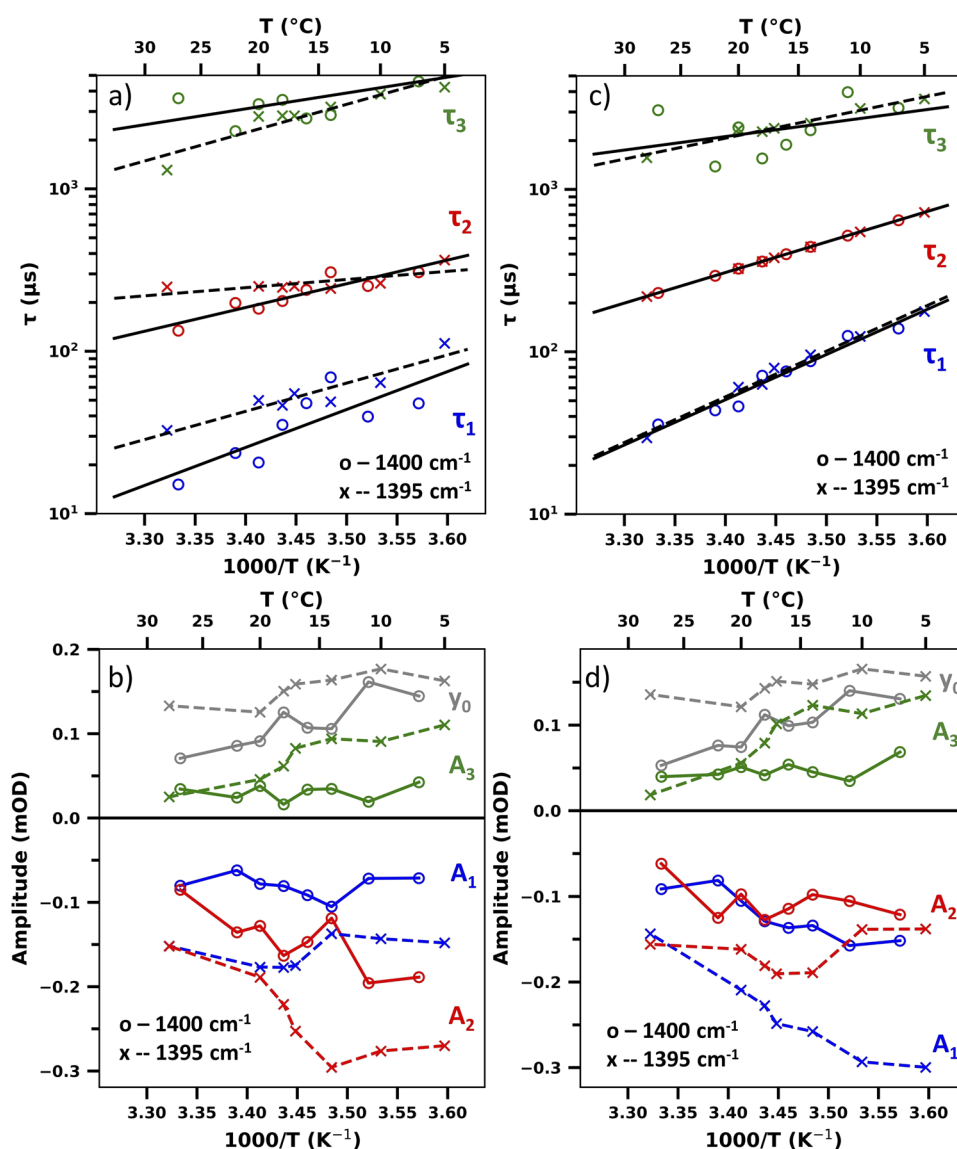


FIG. 5. Temperature dependence of the time constants and amplitudes obtained by three-exponential simulation of the second-flash IR transients ($S_2 \rightarrow S_3$) at 1400 cm^{-1} (circles) and 1395 cm^{-1} (crosses). The two microsecond components are shown in blue (τ_1, A_1) and red (τ_2, A_2), and the slower millisecond-component is shown in green (τ_3, A_3). (a) Arrhenius plot of the time constants obtained from an unconstrained fit. The solid and dotted lines result from a fit (linear regression) of the time-constant values obtained at 1400 cm^{-1} and 1395 cm^{-1} , respectively. (b) The amplitudes corresponding to the time constants in panel (a), as well as the initial values y_0 (i.e., the amplitude from the respective fit at $t = 0$). (c) Arrhenius plot of the time constants obtained when fixing τ_2 to the temperature-dependent ET rate of the $S_2 \rightarrow S_3$ transition.⁵⁵ (d) Corresponding amplitudes of the time constants in panel (c) and initial fit values (y_0). The corresponding activation energies of (a) and (c) are shown in Table I.

constrained can be improved significantly (Fig. S6) while still giving similar results, i.e., an activation energy of $450 \pm 80\text{ meV}$ at 1400 cm^{-1} and $520 \pm 60\text{ meV}$ at 1395 cm^{-1} (Fig. S7 and Table I). [Fully appropriate simulation of the transients for times faster than $10\text{ }\mu\text{s}$ requires two exponential components, as suggested by visual inspection of Fig. S6 and indicated by the τ_0 values in Fig. S7(a), which “jump” between $\sim 1\text{ }\mu\text{s}$ and $\sim 10\text{ }\mu\text{s}$. The analysis of these fast components and their relation to individual S-state transitions will be addressed in forthcoming studies.]

B. Global analysis of the carboxylate bands between 1410 cm^{-1} and 1390 cm^{-1}

Another attempt to improve the fit results of the biphasic decay was to globally analyze transients recorded for various wavenumbers

ranging from 1410 cm^{-1} to 1390 cm^{-1} . The corresponding datasets were collected at five different temperatures from 7°C to 20°C . The decay-associated spectra (DAS) resulting from global fits with three exponential components, with τ_2 fixed to the ET rate, are shown in Figs. S8(b)–S8(d), while Fig. S8(a) shows the steady-state spectra (average value of the time-independent absorption for $>400\text{ ms}$ after laser-flash application). While the steady-state spectrum shows a sharp peak at 1395 cm^{-1} , just like observed by conventional FTIR for the collection of steady-state spectra,⁷⁰ the DAS are broader, especially the DAS of the ET event (τ_2), and do not match the steady-state spectrum. The Arrhenius plot of the time constants is shown in Fig. S8(e). This analysis revealed an activation energy of $460 \pm 100\text{ meV}$ for the PT event (Table I). A global analysis without fixing the ET rate was inconclusive (not shown): the time constants showed no clear trend, and the resulting activation energies were

TABLE I. Overview of fit results: activation energies as determined from the different analysis approaches, as well as the corresponding time constants at 20 °C. The Arrhenius plots for the unconstrained and fixed ET approach with three exponentials, the four-exponential fixed ET approach, and the global analysis are shown in Figs. 5(a) and 5(c), Fig. S7(a), and Fig. S8(e), respectively. Literature values obtained from UV spectroscopy⁵⁵ and photothermal beam deflection (PBD) experiments^{22,23} are shown for comparison. The error estimations were calculated from the estimated covariance of the parameters as determined by least-squares minimization of the Arrhenius-plot data (see the [supplementary material](#) for more details).

Assignment	τ_1 at 20 °C (μ s)	$E_{a,1}$ (meV)	τ_2 at 20 °C (μ s)	$E_{a,2}$ (meV)
	PT	PT	ET	ET
Unconstrained				
1400 cm^{-1}	26 \pm 7	400 \pm 160	190 \pm 30	280 \pm 60
1395 cm^{-1}	44 \pm 6	330 \pm 70	250 \pm 40	90 \pm 40
Fixed ET				
1400 cm^{-1}	51 \pm 3	550 \pm 40	325	373
1395 cm^{-1}	57 \pm 3	540 \pm 30	325	373
Fixed ET; four-exponential fit (supplementary material)				
1400 cm^{-1}	63 \pm 8	450 \pm 80	325	373
1395 cm^{-1}	57 \pm 5	520 \pm 60	325	373
Global analysis 1390 cm^{-1} –1410 cm^{-1} , fixed ET (supplementary material)				
	47 \pm 7	460 \pm 100	325	373
Previously determined values				
PBD ^{22,23}	35 \pm 10	470 \pm 50	280 \pm 90	
UV ⁵⁵			325 \pm 30	373 \pm 40

thus close to zero. (We note that the signal-to-noise ratio of these spectral data was significantly lower than that of the data shown in Fig. 4 and Fig. S5. For high-quality spectra, the significance of the global fit might be high enough for resolving ET and PT time constants well without constraining the ET rate constant to previously reported values.)

C. Comparison of IR transients at 1400 cm^{-1} of plant membrane particles and cyanobacterial core complexes

Noguchi and co-workers reported, for the $S_2 \rightarrow S_3$ transition of cyanobacterial PSII core complexes from *T. elongatus* (at 10 °C), IR transients at 1400 cm^{-1} simulated with time constants of about 10 μ s, 100 μ s, and 350 μ s.^{43,44} However, the 10 μ s and 100 μ s components did not shape the transients in a clearly visible way and were only observed through the global analysis of transients at 1400 cm^{-1} jointly with 1256 cm^{-1} and 1514 cm^{-1} (as well as 2500 cm^{-1} and 4000 cm^{-1} in Ref. 43). In clear contrast, for PSII membrane particles, we observe strong contributions from kinetic components that precede the electron transfer step at 1400 cm^{-1} and for nearby wavenumbers (see Sec. III).

The divergence between the IR transients we measured for PSII membrane particles prepared from spinach and the cyanobacterial PSII core particle of *T. elongatus* previously reported by Noguchi and co-workers^{43,44} might relate to differences between the used experimental setups, stemming from, e.g., differences in bandwidths of the IR light (16 cm^{-1} in Ref. 44 vs 1 cm^{-1} in our experiment) or temporal resolution. This prompted us to record transients at 1400 cm^{-1} also for *T. elongatus* core particles (Fig. 6).

A comparison of IR transients at 1400 cm^{-1} of PSII membrane particles from spinach and PSII core complexes from *T. elongatus* reveals significant differences, as shown in Fig. 6. While the transient of the $S_2 \rightarrow S_3$ transition of *T. elongatus* can be simulated comparably well in the range from 1 μ s to 2 ms with a single exponential component, it is obvious that at least two components are needed for the spinach transient. A third component would be necessary for a good fit of the signal around 1 μ s (not shown). Judging by visual inspection and the fit results, our data for *T. elongatus* seem to be in agreement with the data reported by Noguchi and co-workers for pH 6.⁴⁴ We thus conclude that there is a real and reproducible difference between PSII membrane particles isolated from spinach and *T. elongatus* PSII core particles that is not explainable by experimental differences: the microsecond processes preceding the ET

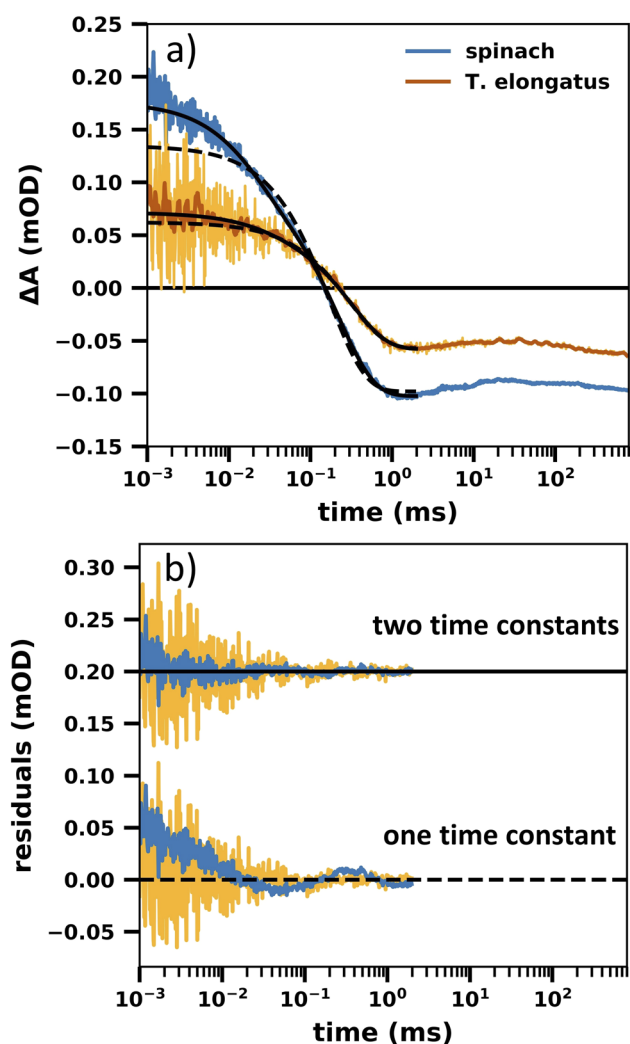


FIG. 6. Comparison of 1400 cm^{-1} transients for PSII membrane particles from spinach (pH 6.2) and PSII core complexes from *T. elongatus* (pH 6.0). Both transients were recorded at 10°C after the second flash initiating the $S_2 \rightarrow S_3$ transition predominantly. (a) Time courses for PSII membrane particles from spinach (blue) and PSII core complexes from *T. elongatus* (orange). The solid lines represent simulations with two decaying exponential components, while the dashed lines represent simulations with only a single decaying exponential component (the simulation parameters are listed in Table SI). The *T. elongatus* data were smoothed using a sliding average to facilitate visual inspection (darker orange). (b) Residuals of the simulations shown in the lower panel.

step in $S_2 \rightarrow S_3$ shape the 1400 cm^{-1} transients strongly only for the spinach PSII membrane particles; relative to the ET component, the amplitude of the faster component is about five times greater for the spinach PSII (Table SI). This difference is especially surprising because the steady-state FTIR difference spectra of the $S_2 \rightarrow S_3$ transition in the region around 1400 cm^{-1} look nearly identical for PSII membrane particles from spinach⁷⁰ and core complexes from *T. elongatus*.³⁶

IV. DISCUSSION

A. Resolving the process preceding electron transfer in the $S_2 \rightarrow S_3$ transition

Here, we report, for PSII membrane particles of spinach, that the IR transients collected at 1395 cm^{-1} and 1400 cm^{-1} strongly reflect several processes that precede the electron transfer step of the $S_2 \rightarrow S_3$ transition, occurring in the sub-microsecond and microsecond time domains. In our analysis, we focus on the pre-ET process proceeding within tens of microseconds, which is presumably associated with the proton-removal process previously suggested by PBD experiments (and thus, in this work, it is denoted as the PT step).

Despite the fact that the IR transients exhibit pronounced changes within $10\text{ }\mu\text{s}$ – $100\text{ }\mu\text{s}$ (PT) and within $100\text{ }\mu\text{s}$ – $1000\text{ }\mu\text{s}$ (ET), unambiguous determination of the corresponding rate constants is not easily achieved. The unconstrained fitting approach resulted in a time constant for the ET step of about $280\text{ }\mu\text{s}$ at 10°C [Fig. 5(a)]. However, the activation energies gained from the unconstrained approach (PT: 330 meV – 400 meV , ET: 190 meV – 250 meV) are not in agreement with previous experiments (PT: 470 meV ,²² ET: 373 meV ⁵⁵) and, more importantly, show a discrepancy between the IR transients at 1395 cm^{-1} and 1400 cm^{-1} . The core of this problematic analysis issue is that when fitting a multi-phasic decay, the amplitudes and time constants of the various exponential component retrieved by curve-fitting are highly correlated: a shift of one time constant is easily compensated by a shift in the other, coupled to pronounced variations of the amplitudes. To our surprise, here, we encounter this basically well-known correlation problem even for exponential components with time constants that differ by almost one order of magnitude. The correlation problem became evident only because the unbiased simulations of the individual transients did not result in a coherent set of time constants for the determination of activation energies for the ET and PT steps. We note that by the multi-exponential simulation of a single transient, the correlation problem may be easily overlooked, *inter alia* because of (unreasonably) low uncertainty ranges for the fit parameters typically provided by standard data analysis software.

The parameter correlation problem originates from too many variable simulation parameters. Therefore, we constrained the fit by enforcing that one time constant (τ_2) matches the known ET rates, aiming at increased significance of the PT time constants (τ_1). In addition, indeed, this approach results in strikingly similar PT time constants for 1395 cm^{-1} and 1400 cm^{-1} transients, throughout the investigated temperature range [Fig. 5(c)], strongly suggesting that the selected simulation approach is adequate, and the resulting activation energy of the PT step is meaningful.

The residuals of the unconstrained approach had been moderately more favorable, especially in the fast time domain, than for the constrained approach, which could relate to an additional fast component not covered by the three-exponential fit. Therefore, we explored the constrained fit approach with an additional fast component and an extended fit range (Figs. S6 and S7). The residuals in the time range of interest improved significantly, but at the price of a degraded agreement between the PT time constants determined for the 1395 cm^{-1} and 1400 cm^{-1} transients, testifying again that very small residuals do not necessarily characterize the most meaningful simulation approach.

In time-resolved spectroscopy, a prominent strategy to overcome the parameter correlation problem of multi-exponential simulations is the collection of transients at various wavenumbers and their joint fit (global analysis) using the same time constants for all transients so that the amplitudes provide decay-associated spectra. We consider this approach generally promising also for the analysis of IR transients of PSII, but it failed for the here analyzed dataset, likely because of insufficient data quality and spectral range. Reasonable results were again obtained only by constraining the ET rate constant in the global analysis (Fig. S8).

Noguchi and co-workers reported IR transients at 1400 cm^{-1} , which they simulated involving time constants of about $10\text{ }\mu\text{s}$, $100\text{ }\mu\text{s}$, and $350\text{ }\mu\text{s}$, for PSII core complexes from *T. elongatus* at $10\text{ }^\circ\text{C}$.^{43,44} However, the $100\text{ }\mu\text{s}$ component in the 1400 cm^{-1} transients was resolvable only through the global analysis, jointly with the 1256 cm^{-1} and 1514 cm^{-1} transients (as well as 2500 cm^{-1} and 4000 cm^{-1} in Ref. 43). Not aiming at decay-associated spectra, they elegantly solved the parameter correlation problem by the joint simulation of a limited number of IR transients collected at selected, especially informative wavenumbers with pronouncedly different time courses. Whether the $100\text{ }\mu\text{s}$ process of their analysis corresponds to the proton removal process previously concluded from PBD experiments is still unclear. In stark contrast to the PBD results,^{22,23} they did neither observe a large kinetic isotope effect for the $100\text{ }\mu\text{s}$ phase nor a strong pH-effect and thus did not attribute this phase to a proton transfer process. Instead, they assigned the $100\text{ }\mu\text{s}$ phase to changes in the hydrogen-bonding interactions of the tyrosine radical (Y_z^\bullet).⁴⁴

In summary, coherent simulation results [Figs. 5(c) and 5(d)] result from the employment of the three-exponential simulations with the time constants of the ET step of the $S_2 \rightarrow S_3$ transition constrained to previously determined values. Within the error limits, identical room-temperature time constants and activation energies suggest that the τ_2 -processes correspond to the proton-removal step concluded from the analysis of PBD results^{22,23} (see Table I). We note that the agreement in the activation energies is especially compelling as the value of $\sim 500\text{ meV}$ is larger than for any other process in the S-state cycle of PSII. Additional evidence could come from the analysis of the kinetic isotope effect in the IR transients, which is complicated by the parameter-correlation problem of the multi-exponential time courses discussed further above; preliminary results suggest a sizable kinetic isotope effect (Mäusle *et al.*, work in progress).

B. Difference between *T. elongatus* and spinach PSII

There is a major and fully reproducible difference in the IR transients at 1400 cm^{-1} between cyanobacterial PSII core complexes prepared from *T. elongatus* cells and PSII membrane particles prepared from spinach leaves: While for the spinach PSII, the pre-ET phase contributes strongly to the IR transients of the $S_2 \rightarrow S_3$ transition, it exhibits a much smaller amplitude in the cyanobacterial sample. This difference might result from bands that are at higher or lower wavenumbers in the two types of PSII samples, e.g., due to different local environments of residues involved in the pre-ET events. The high level of sequence homology between plant and cyanobacterial PSII for residues in the vicinity of the active-site metal complex disfavors the band-shift explanation. However, comparative

analyses of IR transients covering an extended range of wavenumbers, for both organisms, are required to exclude the band-shift explanation rigorously.

The pronounced difference in the amplitude of the pre-ET phase could relate to differences between PSII proteins from thermophilic and non-thermophilic organisms. The PSII proteins from the thermophilic cyanobacterium *T. elongatus*, which has an optimal growth temperature of about $57\text{ }^\circ\text{C}$,⁷¹ are expected to be more rigid at $10\text{ }^\circ\text{C}$ than spinach PSII proteins (for a general review on protein stability and flexibility, see Ref. 72). At comparably high rigidity, less pronounced conformational changes during the pre-ET phase might lead to less pronounced changes in the IR signal. If a small pre-ET amplitude in the IR transient was associated with low mobility of the PSII proteins, however, we would expect a clear trend of increasing pre-ET amplitude in spinach with increasing temperature, which we observed for none of our analysis approaches. Our favored data-analysis approach indeed suggests a pronounced temperature dependence of the pre-ET phase, but its amplitude increases with a decrease in temperature [Fig. 5(d)] thereby disfavoring a simple relation between protein mobility and amplitude of the pre-ET phase. Future comparative investigation of PSII core complexes from thermophilic and non-thermophilic cyanobacteria could clarify the relation between pre-ET step and thermophilicity.

Aside from the stark differences in the amplitudes of the pre-ET phase, there may be a difference in the ET rates when comparing the two types of PSII. We note that to obtain the simulation results of Table SI, we did *not* use an approach where increased significance of the simulation parameters is achieved by an ET rate constant fixed to literature values, which likely corrupts the rate-constant value for the ET of PSII membrane particles seriously, but may result in proper values for *T. elongatus* PSII because of negligible interferences with the minor contribution of the pre-ET step to the IR transients in *T. elongatus* (see preceding paragraph). We conclude that our analysis is in line with an $S_2 \rightarrow S_3$ ET time constant at $10\text{ }^\circ\text{C}$ of about $320\text{ }\mu\text{s}$ in PSII of the thermophilic cyanobacterium but about $550\text{ }\mu\text{s}$ in spinach PSII.

The ET time constant of $550\text{ }\mu\text{s}$ determined by Renger and Hanssum at $10\text{ }^\circ\text{C}$ by the analysis of near-UV absorption transients for spinach PSII membrane particles⁵⁵ is compatible with our rate-constant analysis of the IR transients for spinach PSII. However, it is significantly slower than the value of $320\text{ }\mu\text{s}$ we determined for *T. elongatus*, the value of $350\text{ }\mu\text{s}$ reported by Noguchi and co-workers⁴⁴ for *T. elongatus*, and the value of about $320\text{ }\mu\text{s}$ reported by Renger and co-workers⁷³ for *T. vulcanus*. (PSII of *T. elongatus* and PSII of *T. vulcanus* are essentially sequence-identical, and the same rate-constant values are expected.) The faster reaction rate in thermophilic PSII contrasts with findings for other proteins from thermophiles, for which a higher rigidity comes hand in hand with lower catalytic rates.⁷² Interestingly, also the activation energy of the $S_2 \rightarrow S_3$ electron transfer step has been reported to be different (lower) in PSII prepared from the thermophilic cyanobacterium *T. vulcanus*.⁷⁴ Boussac and co-workers⁷⁵ have shown that expressing different naturally occurring D1-variants in *T. elongatus* affects the ET rate between Y_z and P680. In conclusion, there are reproducible differences in the ET rate constants that may be explainable by differences in the PSII proteins when comparing (mesophilic) plant PSII and thermophilic cyanobacterial PSII. Currently, the

molecular origin of these differences is ill-understood; further investigations are needed for clarification.

C. Relating ET and pre-ET processes of the $S_2 \rightarrow S_3$ transition to IR transients

1. Basic reaction kinetics

The reaction kinetics (rate constant, activation energy, kinetic isotope effect, and pH dependence) of the ET step of the $S_2 \rightarrow S_3$ transition have been well characterized by various methods, in particular, UV-vis^{55,56,65,73,74,76,77} and supported by time-resolved x-ray absorption spectroscopy,^{78,79} a typical time constant (reciprocal rate constant) is 320 μs at 20 °C (Table I). Evidence for a preceding process, taking place within tens of microseconds, came from photothermal beam deflection (PBD) experiments.^{22,23} It was assigned to proton removal from the Mn_4CaO_x complex of PSII by long-distance proton transfer, likely via protein-internal chains of protonatable side chains and water molecules,^{80–82} and coupled to specific structural changes in the active-site Mn_4CaO_x complex.^{19,26} In time-resolved x-ray absorption experiments, a delayed onset of the Mn(III) \rightarrow Mn(IV) oxidation step was observed,⁷⁹ which implies that a pre-ET process, likely the proton-removal step suggested by PBD experiments,^{22,23} is an essential requirement for the subsequent ET step in the $S_2 \rightarrow S_3$ transition.

2. ET step at atomic level

In the $S_2 \rightarrow S_3$ transition, an electron is transferred toward the oxidized tyrosine Y_Z^{ox} residue. Whether this ET step is associated with Mn oxidation or the formation of a ligand radical, e.g., onset of water oxidation by peroxide formation, has been long disputed (see Refs. 9 and 10 for reviews). Starting in 2003, we have provided experimental evidence by x-ray absorption and emission spectroscopy (XAS and XES) that in the $S_2 \rightarrow S_3$ transition, Mn oxidation is coupled to the transformation of five-coordinate Mn(III) to six-coordinate Mn(IV),^{83–86} in line with suggestions based on computational chemistry⁸⁷ and later supported by advanced EPR spectroscopy.⁸⁸ Crystallographic results by Shen and co-workers³⁴ verified the coordination change but were interpreted as evidence for the onset of the O–O bond formation by oxidation of “substrate-water,” which would be in clear conflict with the x-ray spectroscopy results. More recent crystallographic studies, however, provided evidence for a sequence of events that is in line with our earlier conclusion of Mn(III) \rightarrow Mn(IV) oxidation coupled to the filling of an open coordination site by binding of a water species.^{19,26} The crystallographic results furthermore suggest strongly that the filling of the open coordination site does not precede the ET step but occurs concomitantly with Mn oxidation in the ET step.^{19,26} This finding is of importance also regarding the role of protons in ET and pre-ET steps, as outlined in the following.

3. Relation between pre-ET and proton-coupled ET steps

For the $S_2 \rightarrow S_3$ transition, we consider the following scenario as being most plausible: An additional H_2O molecule enters the ligand environment of the Mn_4CaO_x cluster and binds in the form of an OH^- ion, concomitantly with Mn(III) \rightarrow Mn(IV) oxidation and transfer of a proton to a proton accepting group (acceptor base) in

a proton-coupled ET step. The acceptor base previously has been created by deprotonation in a pre-ET step, which is the proton-removal step concluded from PBD experiments. [The coupling of the electron transfer in the $S_2 \rightarrow S_3$ transition to proton transfer has been concluded from a kinetic isotope effect (KIE) upon $\text{H}_2\text{O}/\text{D}_2\text{O}$ exchange, where the rate constant in D_2O was found to be reduced by a factor close to 2, in clear contrast to the other three S-state transitions where only a marginal KIE was detectable.^{23,56,77,79}]

4. Deprotonating group in the pre-ET step

In the $S_2 \rightarrow S_3$ transition, the light-induced formation of Y_Z^{ox} likely causes a pK_a -change and thereby deprotonation in the vicinity of the Mn_4CaO_x cluster. The pK_a change presumably results from electrostatic through-space interactions and/or rearrangement of the H-bonded protein–water networks comprising Y_Z and the Mn_4Ca cluster. However, despite the significant interest regarding the mechanistic understanding of light-driven water oxidation by PSII, neither the de-protonating group nor the rate-determining step has been identified so far. The deprotonating group in the pre-ET step could be as follows:

- (i) a protein side chain in vicinity of the Mn_4CaO_x cluster,
- (ii) a water molecule coordinated to a metal ion of the Mn_4CaO_x cluster, and
- (iii) a protonated water cluster, possibly located between the Mn_4CaO_x cluster and the oxidized tyrosine residue (Y_Z).

5. Direct visibility of pre-ET deprotonation in IR transients around 1400 cm^{-1} ?

Deprotonation of a protein side chain [option (i)] would become directly visible in IR transients. Specifically, for deprotonation of a carboxylate side chain ($\text{Asp/Glu-COOH} \rightarrow \text{Asp/Glu-COO}^- + \text{H}^+$), the here analyzed IR transients might report directly on the deprotonation event because Asp/Glu-COO^- formation is expected to result in an IR absorption increase in the spectral region of symmetric carboxylate vibrations. However, we observed an absorption decrease (negative A_2), which clearly disfavors deprotonation of carboxylate side chains, but cannot exclude it, *inter alia* because only part of the spectral range assignable to the symmetric stretching mode was investigated (1390 cm^{-1} –1410 cm^{-1} in Fig. S8).

It has been suggested in computational studies that the processes in the $S_2 \rightarrow S_3$ transition comprise deprotonation of a water molecule and concurrent transient protonation of a nearby carboxylate side chain.^{89–91} While the direct observation of a carboxylate protonation event could be in line with a negative IR absorption change at 1400 cm^{-1} , we would then expect reversal in the ET phase. Since both the pre-ET and ET phases are associated with a decrease in absorption at 1400 cm^{-1} , however, our data also disfavor a transient carboxylate protonation.

6. Pre-ET deprotonation indirectly reflected in IR transients around 1400 cm^{-1}

Both the deprotonation events of metal–ion coordinated water molecule [option (ii)] or of a protonated water cluster [option

(iii)] are not expected to be directly visible in IR transients around 1400 cm^{-1} because the metal–oxygen vibrations are observable at much lower frequencies (around 500 cm^{-1}), whereas protonated water clusters may be observable as broad IR bands at wavenumbers considerably higher than 1400 cm^{-1} . However, both still could become observable in the region of carboxylate vibrations because of frequency shifts caused by conformational changes (of the carboxylate side chain), modified H-bonding (to the carboxylate side chain), and electric-field effects (electrochromic shift of the carboxylate vibrations).

Rearrangements of H-bonds in conjunction with the deprotonation process are likely to affect the vibrational frequencies of nearby (H-bonded) carboxylates [for option (i), (ii), and (iii)]. Proton removal from the Mn_4CaO_x cluster environment corresponds to a charge change and thus could be associated with short-range and long-range influence on vibrational frequencies. A candidate for conformational changes potentially giving rise to IR absorption changes associated with the pre-ET step is the rearrangement of Glu 189 (of the D1 protein of PSII) already visible in a crystallographic snapshot structure recorded $50\ \mu\text{s}$ after the light flash that induced the $S_2 \rightarrow S_3$ transition.^{19,26} Glu 189 changes from bidentate ligation (to Mn and Ca) to monodentate ligation (to Mn only), which is expected to result in a major frequency shift of the carboxylate vibrations. (We note that it is still unclear whether the Glu 189 rearrangement proceeds concomitantly with the here discussed proton-removal step or before.)

7. Peripheral carboxylate side chains could play a role

Protonation-state changes in carboxylate residues at the PSII periphery may also affect the transients detected close to 1400 cm^{-1} . Junge and co-workers suggested that Y_Z^{ox} formation affects pK_a of peripheral groups by long-range electrostatic interaction, resulting in their deprotonation.^{45,92,93} In the $S_2 \rightarrow S_3$ transition, fast deprotonation of protonated carboxylate (carboxylic acid) side chains at the periphery of the PSII protein complex might be caused by Y_Z^{ox} formation, followed by their re-protonation, concomitantly with proton removal from the environment of the Mn_4CaO_x cluster. If this scenario was relevant, the re-protonation could explain an absorption decrease around 1400 cm^{-1} , concomitantly with the pre-ET process in vicinity of the Mn_4CaO_x cluster.

8. Role of temperature-dependent equilibria

The clear temperature dependence of A_1 , the amplitude of the pre-ET step in the multi-exponential simulation, is remarkable. For a simple sequence of reaction steps, the rate constant should be temperature dependent, but the amplitudes (or at least the amplitude ratios) should be temperature independent. We note that in an attempt to reduce the number of fit parameters, we also approached the simulation with a temperature-independent A_1/A_2 amplitude ratio, resulting in unacceptably poor simulation quality, at several temperatures, thereby confirming the temperature dependence of the amplitude ratio (results not shown). The pronounced temperature dependence of A_1 points to temperature-dependent equilibria of oxidation states, protein conformations, or protonation states. The low amplitude of the pre-ET phase in the 1400 cm^{-1} transients of *T. elongatus* (Fig. 6) may also relate to an equilibrium between

two states, which is shifted to a different state in the PSII core particles of the thermophilic cyanobacterium than in the PSII membrane particles from spinach.

V. CONCLUSION

Driving PSII membrane particles synchronously through the water-oxidation cycle by nanosecond laser-flash sequences, we investigated the light-induced PSII processes by time-resolved single-frequency IR difference spectroscopy in the spectral range of symmetric carboxylate vibrations of protein side chains (Asp/Glu-COO^-). Employing tunable quantum cascade lasers as IR measuring light and an automated sample exchange scheme, which facilitated extensive signal averaging of flash-sequence data recorded for dark-adapted PSII, we find that the collection of high-quality IR transients in the time range from 100 ns to 1 s can be realized with adequate S-state cycling synchronicity. In our analysis, we focus on the microsecond events in the $S_2 \rightarrow S_3$ transition. For the pre-ET step in the $S_2 \rightarrow S_3$ transition of photosynthetic water oxidation, we conclude the following:

1. The IR absorption transients at 1395 cm^{-1} and 1400 cm^{-1} in the time range from $1\ \mu\text{s}$ to 1 ms reflect the pre-ET step, proton-removal step (tens of microseconds), and the ET step (hundreds of microseconds); both steps can be investigated by the analysis of IR transients reflecting carboxylate vibrations.
2. For transients at various temperatures, unconstrained multi-exponential simulations of the individual transient did not provide a coherent set of time constants (reciprocal rate constants). This suggests severe correlations between the fit parameters, despite the time constant values separated by almost one order of magnitude, which leads to erroneous and thus potentially misleading rate constant values.
3. The employment of knowledge-based constraints was required to solve the parameter correlation problem, here being the time-constant value of the $S_2 \rightarrow S_3$ ET step previously determined in independent experiments. A global analysis of spectra collected at various wavenumbers may provide an alternative solution to the parameter-correlation problem but failed for the here analyzed dataset, likely because of insufficient data quality and spectral range.
4. Using a constrained simulation approach, the proton-removal step was resolvable and an exceptionally high activation energy of $540 \pm 30\text{ meV}$ was determined, which agrees within the error limits with the value previously determined by photothermal experiments ($470 \pm 50\text{ meV}$).
5. The proton-removal step clearly seen for PSII membrane particles is, surprisingly, only weakly reflected in the IR transients of PSII core complexes of a thermophilic cyanobacterium (*T. elongatus*), asking for further investigation of this phenomenon.
6. On the basis of previous photothermal experiments, $\text{H}_2\text{O}/\text{D}_2\text{O}$ exchange experiments, and recent crystallographic results, we conclude that the pre-ET step here investigated by time-resolved IR spectroscopy is assignable to deprotonation of a group that is re-protonated concurrently with electron transfer, as detailed in Sec. IV.

- The analyzed IR transients disfavor deprotonation of a carboxylic acid in the pre-ET step but presently cannot exclude it. Similarly, carboxylate protonation in the pre-ET step that is followed by reprotonation in the ET-step is not supported by the analyzed IR transients.
- Clearly, temperature-dependent amplitudes of the proton-removal phase suggest the existence of thermal equilibria that determine how strongly the proton-removal step is reflected at the respective wavenumber in the IR transients. It remains an interesting open question whether these equilibria are also pH-dependent or differ between cyanobacterial core complexes and plant-PSII membrane particles.

SUPPLEMENTARY MATERIAL

See the [supplementary material](#) for additional information on experimental procedures and data analysis, additional IR transients at 1395 cm^{-1} and 1478 cm^{-1} , global analysis of a dataset of transients at several wavenumbers between 1390 cm^{-1} and 1410 cm^{-1} , analysis of the transients at 1395 cm^{-1} , the alternative analysis of the transients at 1400 cm^{-1} , and fit parameters of the analysis of 1400 cm^{-1} transients of *T. elongatus* core complexes.

AUTHORS' CONTRIBUTIONS

S.M.M. and A.A. contributed equally to this work.

ACKNOWLEDGMENTS

We thank the Deutsche Forschungsgemeinschaft (DFG) for financial support from the Collaborative Research Center (SFB 1078) on Protonation Dynamics in Protein Function (Project A4/Dau). We thank Rudolph A. Marcus for his relentless work on electron transfer theory that has shaped our thinking as well as the corresponding experimental strategies when addressing the reactions in photosynthetic water oxidation.

DATA AVAILABILITY

All relevant data are presented in the article or as the [supplementary material](#).

REFERENCES

- H. Dau and I. Zaharieva, *Acc. Chem. Res.* **42**, 1861 (2009).
- J.-R. Shen, *Annu. Rev. Plant Biol.* **66**, 23 (2015).
- D. J. Vinyard and G. W. Brudvig, *Annu. Rev. Phys. Chem.* **68**, 101 (2017).
- W. Junge, *Q. Rev. Biol.* **52**, e1 (2019).
- N. Cox, D. A. Pantazis, and W. Lubitz, *Annu. Rev. Biochem.* **89**, 795 (2020).
- H. Dau, C. Limberg, T. Reier, M. Risch, S. Roggan, and P. Strasser, *ChemCatChem* **2**, 724 (2010).
- J. Barber, *Chem. Soc. Rev.* **38**, 185 (2009).
- W. Lubitz, E. J. Reijerse, and J. Messinger, *Energy Environ. Sci.* **1**, 15 (2008).
- H. Dau and M. Haumann, *Coord. Chem. Rev.* **252**, 273 (2008).
- D. A. Pantazis, *ACS Catal.* **8**, 9477 (2018).
- A. Zouni, H.-T. Witt, J. Kern, P. Fromme, N. Krauss, W. Saenger, and P. Orth, *Nature* **409**, 739 (2001).
- K. N. Ferreira, T. M. Iverson, K. Maghlaoui, J. Barber, and S. Iwata, *Science* **303**, 1831 (2004).
- Y. Umena, K. Kawakami, J.-R. Shen, and N. Kamiya, *Nature* **473**, 55 (2011).
- P. Joliot, G. Barbieri, and R. Chabaud, *Photochem. Photobiol.* **10**, 309 (1969).
- H. Dau and M. Haumann, *Photosynth. Res.* **92**, 327 (2007).
- L. V. Pham and J. Messinger, *Biochim. Biophys. Acta* **1857**, 848 (2016).
- P. Chernev, I. Zaharieva, H. Dau, and M. Haumann, *J. Biol. Chem.* **286**, 5368 (2011).
- H. Dau and M. Haumann, *Science* **312**, 1471 (2006).
- J. Kern, R. Chatterjee, I. D. Young, F. D. Fuller, L. Lassalle, M. Ibrahim, S. Gul, T. Fransson, A. S. Brewster, R. Alonso-Mori, R. Hussein, M. Zhang, L. Douthit, C. de Lichtenberg, M. H. Cheah, D. Shevela, J. Wersig, I. Seuffert, D. Sokaras, E. Pastor, C. Weninger, T. Kroll, R. G. Sierra, P. Aller, A. Butryn, A. M. Orville, M. N. Liang, A. Batyuk, J. E. Koglin, S. Carbajo, S. Boutet, N. W. Moriarty, J. M. Holton, H. Dobbek, P. D. Adams, U. Bergmann, N. K. Sauter, A. Zouni, J. Messinger, J. Yano, and V. K. Yachandra, *Nature* **563**, 421 (2018).
- B. Kok, B. Forbush, and M. McGloin, *Photochem. Photobiol.* **11**, 457 (1970).
- H. Dau and M. Haumann, *Biochim. Biophys. Acta* **1767**, 472 (2007).
- A. Klauss, M. Haumann, and H. Dau, *Proc. Natl. Acad. Sci. U. S. A.* **109**, 16035 (2012).
- A. Klauss, M. Haumann, and H. Dau, *J. Phys. Chem. B* **119**, 2677 (2015).
- J. Messinger, M. Badger, and T. Wydrzynski, *Proc. Natl. Acad. Sci. U. S. A.* **92**, 3209 (1995).
- N. Cox and J. Messinger, *Biochim. Biophys. Acta* **1827**, 1020 (2013).
- M. Ibrahim, T. Fransson, R. Chatterjee, M. H. Cheah, R. Hussein, L. Lassalle, K. D. Sutherlin, I. D. Young, F. D. Fuller, S. Gul, I. S. Kim, P. S. Simon, C. de Lichtenberg, P. Chernev, I. Bogacz, C. C. Pham, A. M. Orville, N. Saichek, T. Northen, A. Batyuk, S. Carbajo, R. Alonso-Mori, K. Tono, S. Owada, A. Bhowmick, R. Bolotovskiy, D. Mendez, N. W. Moriarty, J. M. Holton, H. Dobbek, A. S. Brewster, P. D. Adams, N. K. Sauter, U. Bergmann, A. Zouni, J. Messinger, J. Kern, V. K. Yachandra, and J. Yano, *Proc. Natl. Acad. Sci. U. S. A.* **117**, 12624 (2020).
- C. de Lichtenberg and J. Messinger, *Phys. Chem. Chem. Phys.* **22**, 12894 (2020).
- J. Barber, K. Ferreira, K. Maghlaoui, and S. Iwata, *Phys. Chem. Chem. Phys.* **6**, 4737 (2004).
- B. Loll, J. Kern, W. Saenger, A. Zouni, and J. Biesiadka, *Nature* **438**, 1040 (2005).
- M. Suga, F. Akita, K. Hirata, G. Ueno, H. Murakami, Y. Nakajima, T. Shimizu, K. Yamashita, M. Yamamoto, H. Ago, and J.-R. Shen, *Nature* **517**, 99 (2015).
- J. Kern, R. Alonso-Mori, R. Tran, J. Hattne, R. J. Gildea, N. Echols, C. Glockner, J. Hellmich, H. Laksmono, R. G. Sierra, B. Lassalle-Kaiser, S. Koroidov, A. Lampe, G. Han, S. Gul, D. DiFiore, D. Milathianaki, A. R. Fry, A. Miahnahri, D. W. Schafer, M. Messerschmidt, M. M. Seibert, J. E. Koglin, D. Sokaras, T. C. Weng, J. Sellberg, M. J. Latimer, R. W. Grosse-Kunstleve, P. H. Zwart, W. E. White, P. Glatzel, P. D. Adams, M. J. Bogan, G. J. Williams, S. Boutet, J. Messinger, A. Zouni, N. K. Sauter, V. K. Yachandra, U. Bergmann, and J. Yano, *Science* **340**, 491 (2013).
- C. Kupitz, S. Basu, I. Grotjohann, R. Fromme, N. A. Zatsepin, K. N. Rendek, M. S. Hunter, R. L. Shoeman, T. A. White, D. Wang, D. James, J.-H. Yang, D. E. Cobb, B. Reeder, R. G. Sierra, H. Liu, A. Barty, A. L. Aquila, D. Deponte, R. A. Kirian, S. Bari, J. J. Bergkamp, K. R. Beyerlein, M. J. Bogan, C. Caleman, T.-C. Chao, C. E. Conrad, K. M. Davis, H. Fleckenstein, L. Galli, S. P. Hau-Riege, S. Kassemeyer, H. Laksmono, M. Liang, L. Lomb, S. Marchesini, A. V. Martin, M. Messerschmidt, D. Milathianaki, K. Nass, A. Ros, S. Roy-Chowdhury, K. Schmidt, M. Seibert, J. Steinbrener, F. Stellato, L. Yan, C. Yoon, T. A. Moore, A. L. Moore, Y. Pushkar, G. J. Williams, S. Boutet, R. B. Doak, U. Weierstall, M. Frank, H. N. Chapman, J. C. H. Spence, and P. Fromme, *Nature* **513**, 261 (2014).
- J. Kern, R. Tran, R. Alonso-Mori, S. Koroidov, N. Echols, J. Hattne, M. Ibrahim, S. Gul, H. Laksmono, R. G. Sierra, R. J. Gildea, G. Han, J. Hellmich, B. Lassalle-Kaiser, R. Chatterjee, A. S. Brewster, C. A. Stan, C. Glockner, A. Lampe, D. DiFiore, D. Milathianaki, A. R. Fry, M. M. Seibert, J. E. Koglin, E. Gallo, J. Uhlig, D. Sokaras, T. C. Weng, P. H. Zwart, D. E. Skinner, M. J. Bogan,

- M. Messerschmidt, P. Glatzel, G. J. Williams, S. Boutet, P. D. Adams, A. Zouni, J. Messinger, N. K. Sauter, U. Bergmann, J. Yano, and V. K. Yachandra, *Nat. Commun.* **5**, 4371 (2014).
- ³⁴M. Suga, F. Akita, M. Sugahara, M. Kubo, Y. Nakajima, T. Nakane, K. Yamashita, Y. Umena, M. Nakabayashi, T. Yamane, T. Nakano, M. Suzuki, T. Masuda, S. Inoue, T. Kimura, T. Nomura, S. Yonekura, L.-J. Yu, T. Sakamoto, T. Motomura, J.-H. Chen, Y. Kato, T. Noguchi, K. Tono, Y. Joti, T. Kameshima, T. Hatsui, E. Nango, R. Tanaka, H. Naitow, Y. Matsuura, A. Yamashita, M. Yamamoto, O. Nureki, M. Yabashi, T. Ishikawa, S. Iwata, and J.-R. Shen, *Nature* **543**, 131 (2017).
- ³⁵A. Barth, *Biochim. Biophys. Acta* **1767**, 1073 (2007).
- ³⁶T. Noguchi, *Photosynth. Res.* **91**, 59 (2007).
- ³⁷T. Noguchi, *Coord. Chem. Rev.* **252**, 336 (2008).
- ³⁸R. J. Debus, *Coord. Chem. Rev.* **252**, 244 (2008).
- ³⁹R. J. Debus, *Biochim. Biophys. Acta* **1847**, 19 (2015).
- ⁴⁰T. Noguchi, H. Suzuki, M. Tsuno, M. Sugiura, and C. Kato, *Biochemistry* **51**, 3205 (2012).
- ⁴¹S. Nakamura and T. Noguchi, *Proc. Natl. Acad. Sci. U. S. A.* **113**, 12727 (2016).
- ⁴²R. J. Service, W. Hillier, and R. J. Debus, *Biochemistry* **49**, 6655 (2010).
- ⁴³H. Sakamoto, T. Shimizu, R. Nagao, and T. Noguchi, *J. Am. Chem. Soc.* **139**, 2022 (2017).
- ⁴⁴H. Takemoto, M. Sugiura, and T. Noguchi, *Biochemistry* **58**, 4276 (2019).
- ⁴⁵W. Junge, M. Haumann, R. Ahlbrink, A. Mulikdjanian, and J. Clausen, *Philos. Trans. R. Soc. B* **357**, 1407 (2002).
- ⁴⁶A. Klauss, T. Sikora, B. Süß, and H. Dau, *Biochim. Biophys. Acta* **1817**, 1196 (2012).
- ⁴⁷G. C. Dismukes and Y. Siderer, *Proc. Natl. Acad. Sci. U. S. A.* **78**, 274 (1981).
- ⁴⁸D. A. Pantazis, W. Ames, N. Cox, W. Lubitz, and F. Neese, *Angew. Chem., Int. Ed.* **51**, 9935 (2012).
- ⁴⁹V. Krewald, M. Retegan, N. Cox, J. Messinger, W. Lubitz, S. DeBeer, F. Neese, and D. A. Pantazis, *Chem. Sci.* **6**, 1676 (2015).
- ⁵⁰V. Krewald, M. Retegan, F. Neese, W. Lubitz, D. A. Pantazis, and N. Cox, *Inorg. Chem.* **55**, 488 (2016).
- ⁵¹D. Bovi, D. Narzi, and L. Guidoni, *Angew. Chem., Int. Ed.* **52**, 11744 (2013).
- ⁵²M. Retegan, V. Krewald, F. Mamedov, F. Neese, W. Lubitz, N. Cox, and D. A. Pantazis, *Chem. Sci.* **7**, 72 (2016).
- ⁵³M. Capone, D. Narzi, D. Bovi, and L. Guidoni, *J. Phys. Chem. Lett.* **7**, 592 (2016).
- ⁵⁴M. Askerka, G. W. Brudvig, and V. S. Batista, *Acc. Chem. Res.* **50**, 41 (2017).
- ⁵⁵G. Renger and B. Hanssum, *FEBS Lett.* **299**, 28 (1992).
- ⁵⁶M. Haumann, O. Bögershausen, D. Cherepanov, R. Ahlbrink, and W. Junge, *Photosynth. Res.* **51**, 193 (1997).
- ⁵⁷H. Schiller and H. Dau, *J. Photochem. Photobiol. B* **55**, 138 (2000).
- ⁵⁸D. A. Berthold, G. T. Babcock, and C. F. Yocum, *FEBS Lett.* **134**, 231 (1981).
- ⁵⁹J. Kern, B. Loll, C. Lüneberg, D. DiFiore, J. Biesiadka, K.-D. Irrgang, and A. Zouni, *Biochim. Biophys. Acta* **1706**, 147 (2005).
- ⁶⁰M. Sugiura, A. Boussac, T. Noguchi, and F. Rappaport, *Biochim. Biophys. Acta* **1777**, 331 (2008).
- ⁶¹R. J. Debus, *Biochemistry* **53**, 2941 (2014).
- ⁶²V. P. Shinkarev, *Biophys. J.* **85**, 435 (2003).
- ⁶³D. J. Vinyard and G. W. Brudvig, *Biochemistry* **54**, 622 (2015).
- ⁶⁴H. Suzuki, M. Sugiura, and T. Noguchi, *J. Am. Chem. Soc.* **131**, 7849 (2009).
- ⁶⁵J. P. Dekker, J. J. Plijter, L. Ouwehand, and H. J. van Gorkom, *Biochim. Biophys. Acta* **767**, 176 (1984).
- ⁶⁶F. Müh, C. Glöckner, J. Hellmich, and A. Zouni, *Biochim. Biophys. Acta* **1817**, 44 (2012).
- ⁶⁷R. de Wijn and H. J. van Gorkom, *Biochemistry* **40**, 11912 (2001).
- ⁶⁸K. Zimmermann, M. Heck, J. Frank, J. Kern, I. Vass, and A. Zouni, *Biochim. Biophys. Acta* **1757**, 106 (2006).
- ⁶⁹R. Ashizawa and T. Noguchi, *Phys. Chem. Chem. Phys.* **16**, 11864 (2014).
- ⁷⁰N. Schuth, Z. Liang, M. Schönborn, A. Kussicke, R. Assunção, I. Zaharieva, Y. Zilliges, and H. Dau, *Biochemistry* **56**, 6240 (2017).
- ⁷¹K. Onai, M. Morishita, S. Itoh, K. Okamoto, and M. Ishiura, *J. Bacteriol.* **186**, 4972 (2004).
- ⁷²P. A. Fields, *Comp. Biochem. Physiol. A: Mol. Integr. Physiol.* **129**, 417 (2001).
- ⁷³H. Koike, B. Hanssum, Y. Inoue, and G. Renger, *Biochim. Biophys. Acta* **893**, 524 (1987).
- ⁷⁴M. Karge, K.-D. Irrgang, and G. Renger, *Biochemistry* **36**, 8904 (1997).
- ⁷⁵M. Sugiura, Y. Ozaki, M. Nakamura, N. Cox, F. Rappaport, and A. Boussac, *Biochim. Biophys. Acta* **1837**, 1922 (2014).
- ⁷⁶F. Rappaport, M. Blanchard-Desce, and J. Lavergne, *Biochim. Biophys. Acta* **1184**, 178 (1994).
- ⁷⁷L. Gerencser and H. Dau, *Biochemistry* **49**, 10098 (2010).
- ⁷⁸M. Haumann, P. Liebisch, C. Muller, M. Barra, M. Grabolle, and H. Dau, *Science* **310**, 1019 (2005).
- ⁷⁹I. Zaharieva, H. Dau, and M. Haumann, *Biochemistry* **55**, 6996 (2016).
- ⁸⁰A.-N. Bondar and H. Dau, *Biochim. Biophys. Acta* **1817**, 1177 (2012).
- ⁸¹A. Gabdulkhakov, A. Guskov, M. Broser, J. Kern, F. Muh, W. Saenger, and A. Zouni, *Structure* **17**, 1223 (2009).
- ⁸²F. M. Ho, *Biochim. Biophys. Acta* **1817**, 106 (2012).
- ⁸³H. Dau, P. Liebisch, and M. Haumann, *Anal. Bioanal. Chem.* **376**, 562 (2003).
- ⁸⁴P. Liebisch, M. Haumann, and H. Dau, *Phys. Scr.* **T115**, 859 (2005).
- ⁸⁵I. Zaharieva, P. Chernev, G. Berggren, M. Anderlund, S. Styring, H. Dau, and M. Haumann, *Biochemistry* **55**, 4197 (2016).
- ⁸⁶N. Schuth, I. Zaharieva, P. Chernev, G. Berggren, M. Anderlund, S. Styring, H. Dau, and M. Haumann, *Inorg. Chem.* **57**, 10424 (2018).
- ⁸⁷P. E. M. Siegbahn, *Chem. Eur. J.* **14**, 8290 (2008).
- ⁸⁸N. Cox, M. Retegan, F. Neese, D. A. Pantazis, A. Boussac, and W. Lubitz, *Science* **345**, 804 (2014).
- ⁸⁹D. Narzi, D. Bovi, and L. Guidoni, *Proc. Natl. Acad. Sci. U. S. A.* **111**, 8723 (2014).
- ⁹⁰P. E. M. Siegbahn, *Phys. Chem. Chem. Phys.* **14**, 4849 (2012).
- ⁹¹K. Kawashima, T. Takaoka, H. Kimura, K. Saito, and H. Ishikita, *Nat. Commun.* **9**, 1247 (2018).
- ⁹²M. Haumann and W. Junge, *Biochemistry* **33**, 864 (1994).
- ⁹³O. Bögershausen and W. Junge, *Biochim. Biophys. Acta* **1230**, 177 (1995).